ACS Catalysis
Research Article
Cite This: ACS Catal. 2018, 8, 4257−4265
pubs.acs.org/acscatalysis

Enhanced Activity Promoted by CeO_x on a CoO_x Electrocatalyst for the Oxygen Evolution Reaction

Jun-Hyuk Kim,[†] Kihyun Shin,[‡,§] Kenta Kawashima,[‡] Duck Hyun Youn,[⊥] Jie Lin,[†,#] Tae Eun Hong,[†,∇] Yang Liu,[†,○] Bryan R. Wygant,[‡] Joy Wang,[†] Graeme Henkelman,[‡,§] and C. Buddie Mullins*,[†,‡,∥]

[†]McKetta Department of Chemical Engineering, [‡]Department of Chemistry, [§]Institute for Computational Engineering and Sciences, and [∥]Texas Materials Institute, University of Texas at Austin, Austin, Texas 78712, United States

[⊥]Department of Chemical Engineering, Kangwon National University, Gangwondaehak-gil, Chuncheon, Gangwon-do 24341, South Korea

[#]Pen-Tung Sah Micro-Nano Science and Technology Institute, Xiamen University, Xiamen, Fujian 361006, People's Republic of China

[∇]Busan Center, Korea Basic Science Institute, Busan 46742, South Korea

[○]College of Chemistry and Chemical Engineering, Central South University, Changsha 410083, People's Republic of China

Supporting Information

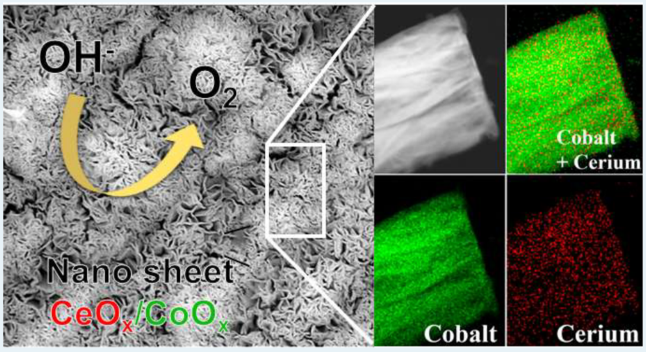

ABSTRACT: Included among the many challenges regarding renewable energy technology are improved electrocatalysts for the oxygen evolution reaction (OER). In this study, we report a novel bifunctional electrocatalyst based on a highly dense CoO_x catalyst by introducing CeO_x. The CoO_x catalyst is fabricated by two-step electrodeposition, including Co seed formation, to obtain a very dense, layered structure, and CeO_x is also successfully deposited on the CoO_x catalyst. CoO_x is an active catalyst showing good activity (η = 0.331 V at 10 mA cm^{-2}) and also stability for the OER. Higher activity is observed with the CeO_x/CoO_x electrocatalyst (η = 0.313 V at 10 mA cm^{-2}). From mechanistic studies conducted with synchrotron-based photoemission electron spectroscopy and DFT calculations, Ce promotes a synergistic effect by perturbing the electronic structure of surface Co species (facile formation to CoOOH) on the CoO_x catalyst and optimizes the binding energy of intermediate oxygenated adsorbates.

KEYWORDS: *cobalt, cerium, electrocatalyst, oxygen evolution reaction, synchrotron*

INTRODUCTION

Rising concerns about climate change and greater use of fossil fuels such as coal, natural gas, and petroleum has given rise to significant attention to renewable energy technology. Among the different approaches, water splitting has received a great deal of attention as a promising potential source of pollution-free fuels. This system consists of two different parts: the cathode, which involves the hydrogen evolution reaction (HER), and the anode, for the oxygen evolution reaction (OER). Since the OER has relatively sluggish kinetics governed by four-electron-transfer processes and complicated adsorption behavior of the intermediates on the electrode in comparison to the HER,[1] much effort has been devoted to increasing OER kinetics via testing of different electrocatalyst materials, including various combinations of metal oxides,[2−6] perovskites,[7,8] sulfides,[9,10] phosphides,[11−14] and selenides.[15−17] Layered metal hydroxides (LMHs), including layered single-metal hydroxides (LSHs) and layered double-metal hydroxides (LDHs), have been widely studied for practical application because of their high performance as electrocatalysts.[18] For instance, LDHs (such as CoCo, NiCo, and NiFe) exhibit significantly higher OER activity in comparison to a noble-metal oxide (such as IrO_2), which is ascribed to enhanced active sites and electronic conductivity.[19]

Investigators have also studied the bifunctionality (or synergistic effect) between the (hydroxyl)oxide and transition-metal substrates, which is key for highly efficient electrocatalytic reactions.[20] The bifunctional effect was also investigated by Zheng et al.[21] They fabricated Fe-Ni hydroxide covered Pt nanoparticles that increased catalytic oxidation reactions; this was mainly attributed to a synergistic effect. Recently, Vojvodic and Jaramillo et al. introduced Ce into Ni oxide for water oxidation.[22] It was revealed that the $NiCeO_x$

Received: February 28, 2018
Published: April 9, 2018

catalyst can modify the local chemical binding environment, showing highly active performance. After this report, several useful studies of Ce for OER catalysts have since been conducted (e.g., $CeO_2/Ni(OH)_2$,[23] $NiCeO_x$,[24] and FeOOH/CeO_2[25]) to maximize its unique properties, such as its stability in an alkaline electrolyte, facile transition between Ce^{3+} and Ce^{4+}, and an efficient supply of oxygen at reaction sites.[26,27]

In this study, in order to greatly promote OER performance, in situ grown highly dense CoO_x together with CeO_x was applied as an electrocatalyst. The highly dense CoO_x catalyst was fabricated on a Ti substrate, with a simple two-step consecutive electrodeposition procedure, including the Co seed formation step. For the CeO_x/CoO_x catalyst, Ce was electrochemically deposited on the Co catalyst after optimizing the deposition conditions.

■ EXPERIMENTAL SECTION

Substrate Preparation. The CoO_x and CeO_x/CoO_x electrocatalysts were prepared on the substrate, polycrystalline Ti (1/4 in. diameter, 99.99% purity, from Kurt J. Lesker). Ti was polished for 10 min with two different types of sandpaper (#1500 and #2000) in order to obtain a smooth surface. The polished Ti was sonicated with distilled water, acetone, and ethanol in order. Then the Ti was finally rinsed with distilled water for the fabrication of deposited CoO_x catalytic film.

Electrocatalyst Preparation. The CoO_x catalyst was fabricated with a simple two-step consecutive electrodeposition procedure. As a first step (Co seed formation), a constant current of 1.0 mA cm^{-2} was applied for 200 s. To achieve the best CoO_x catalyst, deposition was also conducted under other conditions (0.01, 0.1, 5, and 10 mA cm^{-2}) as shown in Figure S1. For the multistep deposition, additional potential was constantly applied on the Co samples (1 V vs Ag/AgCl for 100 s) without stirring. Then the samples were lightly washed with distilled water for further characterization. The precursors for the Co deposition were cobalt nitrate (1 M, Acros Organics) and sodium nitrate (0.1 M, Puratronic) in distilled water. The CeO_x/CoO_x was fabricated on prepared CoO_x film with cerium nitrate (10 mM, Alfa Aesar) and sodium nitrate (0.1 M) with distilled water. A constant voltage was applied at 0.2 V (vs Ag/AgCl) for 5 s to obtain the CeO_x/CoO_x electrocatalyst. For systematic investigation, we prepared a total of four different CeO_x/CoO_x catalysts with different applied potentials (0.1, 0.2, 0.3, and 0.4 V). The Co oxide sample (mainly Co_3O_4 phase) was prepared as a bulk Co catalyst for OER activity comparison.

Characterization. The surface of the catalytic film was investigated using a scanning electron microscope (SEM, FEI Quanta 650 SEM) without a noble-metal coating. The accelerating voltage was 15 kV with 2 nA of current and ∼10 mm of working distance. The sheet resistance of Co samples were determined using a four-point probe technique (KEITHLEY) at room temperature. The samples were structurally characterized by X-ray diffraction (XRD, XPERT-Pro) equipped with Cu Kα radiation (λ = 1.540598 Å) using an incidence angle of 1° and 40 kV of generator voltage without a monochromator. Additionally, high-resolution transmission electron microscopy (HRTEM, JEOL 2010F) was used to further examine the crystallinity, structure, and high resolution of the morphology. The distribution of elements (Co and Ce) of the catalysts was analyzed by X-ray elemental mapping. An additional elemental distribution study was conducted by using secondary ion mass spectrometry (SIMS, CAMECA 7F with low energy primary O^{2+} gun, impact energy 7.5 keV, KBSI) with RAE Detector (CA:20, FA:1800, Ent, Eng, Ext fully open). High-resolution photoelectron spectroscopy (HR-PES) study was performed at the 7B1 beamline (Pohang Accelerator Laboratory, PAL) to obtain elemental or chemical state distribution at specific photon energy (630 eV for core level or 130 eV for valence band study). All energy data were calibrated with Au foil. XPS spectra were also recorded on a Kratos Axis Ultra DLD spectrometer using monochromatic Al Kα radiation (1486.6 eV) with a spot size of 400 μm, to check the thickness of CeO_x. The chamber pressure employed in the XPS studies was maintained at 1×10^{-10} Torr. A three-electrode configuration was used for the preparation of various catalysts and evaluation of electrochemical behavior with a potentiostat (CHI 660D, CH instruments). This system consists of three main electrodes: working electrode (electrocatalyst), reference electrode (Ag/AgCl in saturated KCl, converted to RHE scale), and counter electrode (Pt mesh). Cyclic voltammetry (CV) was conducted in a voltage range between 0.8 and 0.9 V vs RHE with a scan rates of 10, 20, 50, 100, 200, and 500 mV s^{-1} in 1 M NaOH to calculate capacitance (C_{DL}) and electrochemical surface area (ECSA). The oxygen evolution reaction was evaluated by collecting linear voltage sweep (LSV) data in a voltage range between 1.0 and 1.9 V with a scan rate of 10 mV s^{-1}. All of the data of electrochemical evaluation was corrected with an *iR* compensation (4−5 Ω, 80% of auto measured value from CHI software). We performed GGA-level spin-polarized density functional theory (DFT) calculations using the Vienna ab initio simulation package (VASP).[28] The DFT+U[29] method was utilized to treat localized Ce 4f and Co 3d orbitals with U = 5.0[30] and 3.3,[31] respectively. The Perdew−Burke−Ernzerhof (PBE) functional[32] was chosen to describe electron exchange and correlation. The kinetic energy cut off was set to 400 eV, and the Brillouin zone was sampled with a 2 × 2 × 1 *k*-point mesh following the Monkhorst−Pack scheme. Convergence criteria for the electronic structure and the atomic geometry optimization were set at 10^{-5} eV and 0.01 eV $Å^{-1}$, respectively. We prepared Co_3O_4 slab systems with (110) and (111) surfaces, which are predominately considered for chemical reaction research.[33] The Co_3O_4 (110) slab had repeating units (one repeating unit = two atomic layers) with two fixed bottom repeating units; the Co_3O_4 (111) slab had two repeating units (one repeating unit = six atomic layers) with one repeating bottom unit frozen in its bulk position. Both systems were centered between 10 Å vacuum layers to avoid self-interaction through the periodic boundary conditions. We calculated Gibbs free energies with an applied bias to compare the catalytic activity using the equation

$$\Delta G(U) = \Delta E - \Delta E_{ZPE} - T\Delta S - neU$$

where ΔE is reaction energy, ΔE_{ZPE} represents the zero-point energy correction, ΔS is the difference in entropy, and U is the applied bias. Through this Gibbs free energy equation, we made reaction energy diagrams of the entire reaction pathway to explain the catalytic activity difference caused by the presence of CeO_2 on the Co_3O_4 system.

■ RESULTS AND DISCUSSION

In order to optimize the deposition conditions of the Co catalyst, we attempted to compare the OER performance of various Co catalysts. Figure 1 shows the correlation among sheet resistance, electrochemical double-layer capacitance (calculation details in Figure S2), and the specific activity of

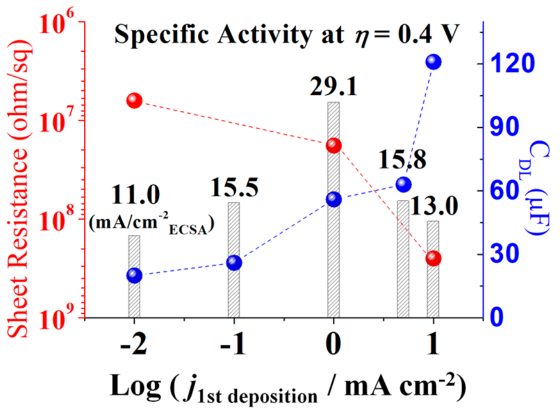

Figure 1. Correlation of the specific activity with the sheet resistance and electrochemical double-layer capacitance (C_{DL}) of the various first steps of Co deposition conditions for the Co-based catalyst.

various Co catalysts for different Co deposition conditions (as the first step of Co electrodeposition). We changed the deposition condition of only the first step (Co seed formation process) and then applied the same deposition conditions (−1 V vs Ag/AgCl for 100 s, as the second step of Co electrodeposition; details in the Supporting Information) for all samples. It was observed that the value for the double-layer capacitance C_{DL} is proportional to the sheet resistance for each Co sample. The Co samples with the lower deposition current exhibited lower sheet resistance and capacitance and vice versa for the higher current conditions. It is speculated that even though the concentration of active sites (related to C_{DL}) increased during higher rate deposition conditions, the loss of conductivity might lead to intrinsic activity degradation. The Co sample prepared at 1 mA cm^{-1} (for the first Co deposition condition) was the tradeoff point for the highest intrinsic activity. With this reason, we have decided to use this condition for synthesis of the highly dense CoO_x catalysts (labeled CoO_x) employed in this study.

XRD was used to investigate the structure of the electrocatalysts as shown in Figure 2A, using a fixed grazing angle of incidence (GIXRD) with an angle of 1°. According to Murthy et al.,[34] the depth of X-ray penetration is less than 1 μm at an incidence angle of 1°; thus, the GIXRD technique enables study of the surface layer of the catalyst, reducing the intense signals from the substrate. The structure of the CoO_x electrocatalyst exhibits an amorphous phase (broad peak near ∼20°), which corresponds to $Co(OH)_2$, with clear peaks related to CoO (220) at 63° and metallic Co-β (110) at 76°. It was expected that the surface would mostly consist of Co oxide/hydroxide and the weak metallic signal at ∼40° comes from the bulk Ti (101) used as the substrate. The CeO_x/CoO_x showed an diffraction pattern almost identical with that of CoO_x, consistent with only surface distribution of Ce species.

The surface morphology of the CoO_x samples was studied by scanning electron microscopy (SEM), as represented in Figure 2B,C. Figure 2B shows the surface of the Co seed film. The main purpose of the first-step deposition is to prepare a seed layer for the dense Co film on the Ti substrate. The density of Co seeds is strongly dependent on the deposition conditions (as shown in Figure S3); there is a lower density Co seed distribution at lower currents for deposition, and vice versa. After the second step of the Co deposition, the substrate is completely covered with a highly dense Co film, which we believe is the best-performing film (Figure 2C).

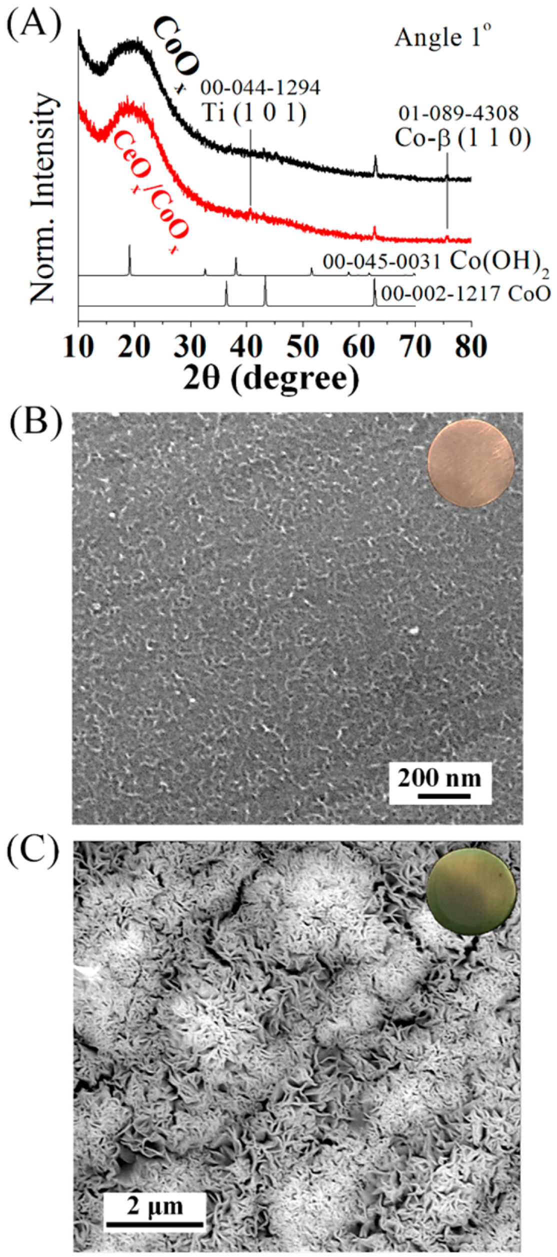

Figure 2. (A) Glancing angle X-ray diffraction pattern of the CoO_x and CeO_x/CoO_x catalysts. SEM images of surface morphology of (B) after the first-step of Co deposition (Co seed) and (C) the CoO_x catalyst (after second-step of Co deposition). Insets in (B, C): catalyst color images.

The Co catalytic film from the less dense Co seed, however, does not entirely cover the substrate (Figure S4a). Although a dense Co film was observed for the higher deposition condition samples (Figure S4d,e) maximizing surface area, a number of hierarchical Co overlayers was also confirmed, which could be the main reason for the loss of conductivity. This phenomenon can be explained by the fact that the Co seed provides a nucleation site for the smaller metastable Co crystallites in the electrolyte.[35] The thickness of the CoO_x film was estimated to be ∼1 μm (Figure S5).

The representative TEM images of the catalysts postsonication are shown in Figure 3. We compared the pristine CoO_x

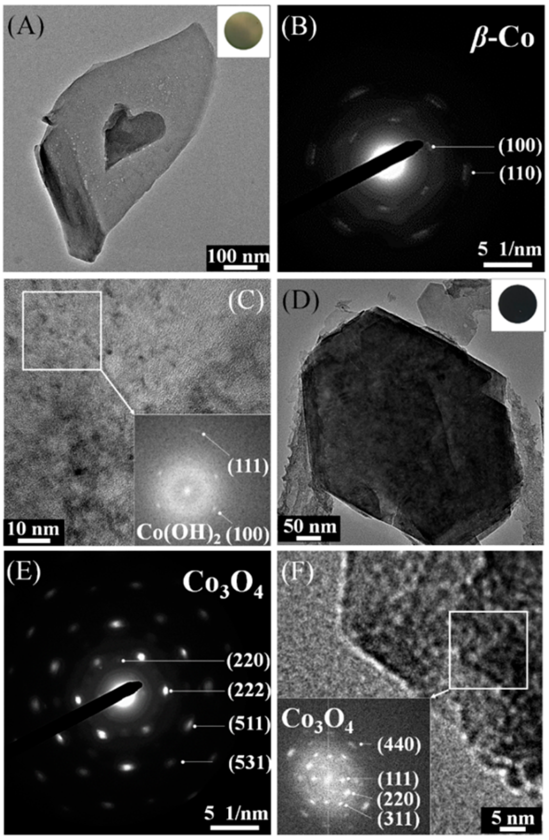

Figure 3. Morphology and SAED pattern images. (A) TEM image, (B) SAED pattern, and (C) HRTEM image of CoO_x. (D) TEM image, (E) SAED pattern, and (F) HRTEM image of CoO_x after the OER scan (after two times of LSV in the range of 1.0 to 1.7 V). Insets: (A, DE) color of their corresponding catalyst surfaces; (C, F) FFT image of their corresponding regions.

and the CoO_x after an OER scan to achieve further insight into the morphology and microstructure. As shown in Figure 3A, the CoO_x catalyst clearly exhibits a sheet morphology. In addition, the distances measured using an SAED pattern (Figure 3B) correspond to metallic β-Co, and a lattice structure related to $Co(OH)_2$ was confirmed by crystal diffraction dots of the FFT pattern (Figure 3C) in HRTEM analysis. These results were further confirmed with HRTEM images (Figure S6a,b). CoO_x is mainly composed of three phases: $Co(OH)_2$, CoO, and metallic Co. This finding is in good agreement with observations from study by XRD. The sheet morphology also appears unchanged after the OER scan (Figure 3D), even though the catalyst turned black. The observed SAED-FFT patterns (Figure 3E,F) clearly match well with the diffraction pattern of Co_3O_4 (#00-009-0418), showing a phase transition after the OER scan. Since the spinel structure of Co_3O_4 is gradually converted to CoOOH and/or Co_2O_3 under an oxidative environment such as OER,[36−38] it is still under the process of structural transition to Co^{3+}-containing species after a single OER scan. With further HRTEM study, other oxide phases (Co_2O_3 and $Co(OH)_2$) were also confirmed (Figure S6c,d).

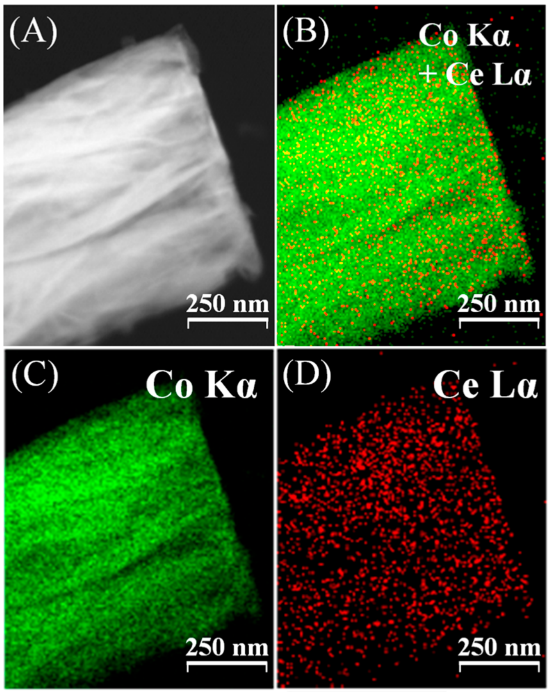

Figure 4. (A) STEM image and (B−D) the corresponding EDS elemental mapping of the CeO_x/CoO_x. The TEM specimen was prepared by sonicating a film-type catalyst with ethanol for 10 min.

Figure 4 shows the elemental mapping images for the CeO_x/CoO_x catalyst. Although we electrochemically deposited Ce on the CoO_x, particles related to Ce were not clearly confirmed by the HRTEM study (Figure S7). Instead, it was revealed that the Ce is homogeneously distributed on the CoO_x sheet with an atomic composition of ∼1% (relative to the ∼99% for Co, Figure S8) by the investigation of elemental mapping. It was determined that the deposition condition is sufficient to evenly distribute Ce on the CoO_x surface: however, not such so as to cause crystallized or extensive growth (the CeO_x thickness was estimated to be below 1.50 nm by calculation of the relative decrease of the Co 2p core level XPS signal; details in Figure S9).

A further check of the Ce distribution on the Co film is conducted from secondary ion mass spectrometry (SIMS) analysis, as represented in Figure 5. SIMS can provide spatial resolution on the scale of micrometers and detect very small amounts of materials with excellent sensitivity and mass resolution.[39] Ce exhibited a concentration of ∼1% relative to Co (∼99%) at the surface for the CeO_x/CoO_x electrocatalyst, while no Ce was detected in the CoO_x catalyst (Figure 5A). In addition, Ce was well distributed over the entire catalytic film with Co (Figure 5B,C); however, the concentration of Ce decreased after ∼1000 s of depth profiling. This might be due to the short deposition time (5 s), which may not have allowed the Ce ion to diffuse deeply enough.

The electrochemical performance was evaluated using rotating disk electrode (TF-RDE) measurements, as shown in Figure 6. Polarization curves for the OER with the catalysts are presented in Figure 6A. Oxidation peaks were rarely observed during the OER scan in view of the large background currents in the region[40] (oxidation can occur because the hydrous Co^{2+} film can be gradually converted to Co^{3+}-containing species such as Co_3O_4, Co_2O_3, and CoOOH). Higher OER activity was observed for the CoO_x film (overpotential, η = 0.331 V at 10 mA cm^{-2}) in comparison to the Co oxide (Co_3O_4) film (η = 0.398 V, mainly Co_3O_4 phase, see Figure S10) and Co seed film (η = 0.413 V). The Co seed film showed the worst performance partially due to the failure to fully cover the electrode surface. The highly dense CoO_x sample exhibits nearly the highest

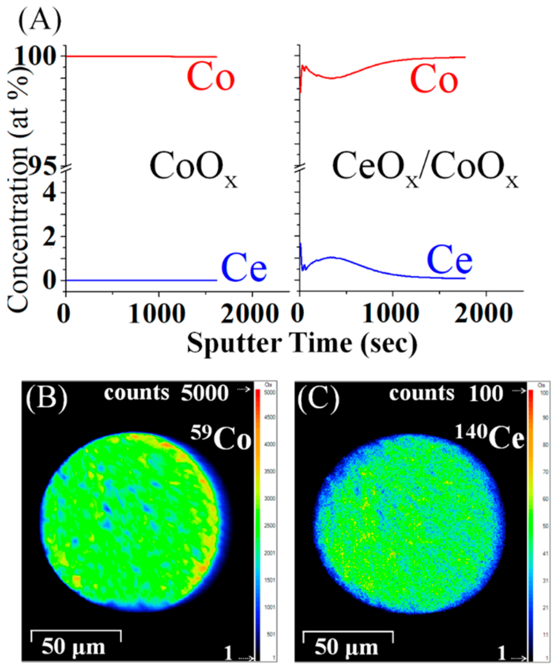

Figure 5. (A) SIMS depth profiling of CoO$_x$, and CeO$_x$/CoO$_x$. 2D images at the surface of the elemental distribution of (B) cobalt and (C) cerium in the CeO$_x$/CoO$_x$ catalyst.

performance of the Co-based sheet-type catalysts (Table S1). The higher surface area from the highly dense morphology could facilitate infiltration of electrolyte into the interior of the CoO$_x$ sheets,[41] bringing out outstanding catalytic activity toward the OER without the limitation of mass transfer in the electrolyte (Figure S11). It is interesting to note that, once Ce was deposited, the overpotential (η = 0.313 V at 10 mA cm^{-2}) was measurably lower for the CeO$_x$/CoO$_x$ catalyst. We also optimized the deposition conditions for Ce to obtain the best CeO$_x$/CoO$_x$ catalyst (optimization details are shown in Figure S12).

The specific and mass activities were also evaluated for all catalysts at η = 0.35 V, as shown in Figure 6B (ECSA calculation details in Figure S13). The highest specific and mass activities were observed with the CeO$_x$/CoO$_x$ catalyst (4.22 mA cm$^{-2}_{\text{ECSA}}$ and 112.7 A g$^{-1}_{\text{metal}}$) among all the samples. The order followed the sequence CoO$_x$ (3.33 mA cm^{-2} $_{\text{ECSA}}$ and 40.95 A g$^{-1}_{\text{metal}}$) > Co seed (0.53 mA cm^{-2} $_{\text{ECSA}}$ and 10.06 A g$^{-1}_{\text{metal}}$) > Co oxide (Co_3O_4, 0.08 mA cm^{-2} $_{\text{ECSA}}$ and 5.11 A g$^{-1}_{\text{metal}}$). The greater intrinsic OER activity in the CoO$_x$ catalyst in comparison to the Co_3O_4 film might be explained by the increase in active sites (including edge sides) and electrical conductivity from the unique sheet type structural characteristics.[19] From this, it can be explained that when we compare the Co_3O_4 and Co seed samples, although the Co seed showed lower OER performance on the basis of geometric area due to the lack of surface coverage, it has higher intrinsic activity (specific and mass activities) on the basis of ECSA and metal loading.

The Tafel slope for various catalysts, which is commonly utilized to evaluate the kinetics of the electrocatalyst, is shown in Figure 6C. Remarkably, the smallest Tafel slope of 66 mV dec^{-1} was achieved for the CeO$_x$/CoO$_x$ catalyst, which shows the best electrocatalytic kinetics and has a better slope than that of the CoO$_x$ sample (70 mV dec^{-1}). Tafel slopes were slightly higher in the Co_3O_4 (80 mV dec^{-1}) and Co seed (96 mV dec^{-1}). The stability was measured by a constant current measurement (Figure 6D), indicating no rapid degradation of the CoO$_x$ and CeO$_x$/CoO$_x$ electrocatalytic films. Overall, the

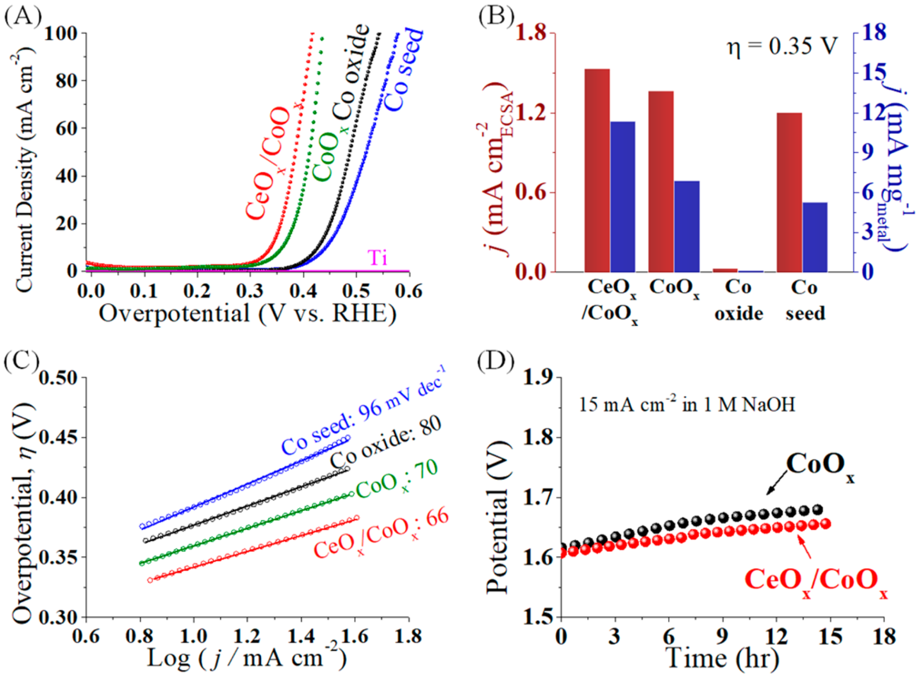

Figure 6. Electrochemical test results of various catalysts. (A) OER polarization curves, (B) specific and mass activity at η = 0.35 V, and (C) Tafel slopes for the Co seed (after 1 step of Co deposition), Co oxide, CoO$_x$, and CeO$_x$/CoO$_x$ catalysts. (D) Chronopotentiometric curves of CoO$_x$ and CeO$_x$/CoO$_x$ at 15 mA cm^{-2}. The performance of Ti (substrate) was evaluated for comparison. The Co oxide was prepared by heat treatment (500 °C for 3 h in air) of polycrystalline Co metal as the same size of Ti (mainly Co_3O_4 phase by Rietveld refinement, Figure S10). The Ti (substrate) can be seen to be inert as a OER catalyst over the entire scan region (from 1.0 to 1.85 V) in this study.

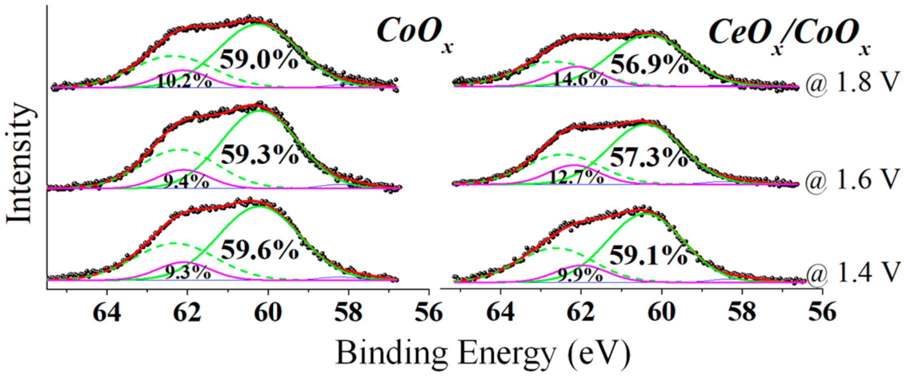

Figure 7. Synchrotron-based photoemission spectroscopy core level spectra of Co 3p for the CoO$_x$ and CeO$_x$/CoO$_x$ catalysts as a function of the applied OER potential (1.4, 1.6, and 1.8 V). The blue solid line represents metallic Co, while the green line signifies CoO $2p_{3/2}$, the pink line represents other oxide species, and the green dotted line represents CoO $2p_{1/2}$ (ΔE[Co $3p_{1/2}$−Co $3p_{3/2}$] = 1.1 eV[42]). The data were collected using a photon energy of 630 eV (an average escape depth of ∼1.0 nm[43]) for the core level. A Shirley background was subtracted from the spectrum before deconvolution. All of the samples were prepared after holding for 10 min at each specific potential for the analysis.

highly dense CoO$_x$ catalyst showed good intrinsic OER activity, and we suggest that the excellent OER performance of the CeO$_x$/CoO$_x$ catalyst results from synergistic effects caused by the addition of CeO$_x$. To elucidate this synergistic effect, the CoO$_x$ and CeO$_x$/CoO$_x$ samples were further studied by high-resolution photoelectron spectroscopy (HR-PES) to investigate the outermost layers of the film.

High-resolution photoemission spectroscopy (HR-PES) analysis was carried out at the Pohang Accelerator Laboratory (PAL, 8A1 beamline) to observe the electronic properties of Co and the valence band (VB) of the CoO$_x$ and CeO$_x$/CoO$_x$ catalysts, as represented in Figures 7 and 8. The Co 3p spectra were measured as a function of the applied potential to look for trends over the OER range (Figure 7). It is important to note that the spectrum of the samples was analyzed at 630 eV for a more surface sensitive analysis. The Co 3p XPS signals can be mainly deconvoluted by the positions of Co metal (at 58.6 eV),[44] CoO (at 60.2 eV), and another Co oxide species. The higher oxidation state of Co species could not be entirely deconvoluted due to similar peak positions among various Co oxide species (e.g., a 1.5 eV shift for CoO in comparison to metallic Co[45] and a slightly higher shift but with a very similar position for other Co oxidation states[46,47] such as Co_2O_3, CoOOH, and $Co(OH)_2$). The main spectral line at 60.2 eV corresponds to Co^{2+} in CoO,[46] while another position for the higher oxidation state of Co is assigned to 62.1 eV. Upon increasing the potential, we can observe a strong decrease in relative area of the CoO peak in comparison to the total fitting area (59.6% to 59.0% for the CoO$_x$ and 59.1% to 56.9% for the CeO$_x$/CoO$_x$), together with an increase in area for the higher oxides for both CoO$_x$ (9.3% at 1.4 V to 10.2% at 1.8 V) and CeO$_x$/CoO$_x$ (9.9% at 1.4 V to 14.6% at 1.8 V). This observation suggests a gradual oxidation of Co species toward high OER potential. Notably, the relative area of CoO was smaller in the CeO$_x$/CoO$_x$ at all the OER potentials (higher oxidation states of Co in the CeO$_x$/CoO$_x$ than the CoO$_x$ catalyst), suggesting a likely change in electronic structure via Ce introduction. This speculation is supported theoretically in which adjacent elements are reported to be electronically perturbed by interactions with Ce.[48] In an oxidation environment, CeO$_x$ is able to promote oxidation reactions due to an increase in the adsorption probability of O_2,[49] and it was revealed from a theoretical study that Ce^{3+} sites at the interface with an another element adsorb O_2, dissociate, and then release atomic O for reaction in an efficient way (or bind O atoms more weakly).[50] Another study reported that O vacancies in the ceria structure can energetically react and dissociate water.[51] On the basis of these unique characteristics of CeO$_x$, research is underway in the OER field. Yano and Sharp et al. recently reported that highly oxidized Co species can play a very active role in OER activity.[52] This same principle holds in another LMHs such as Ni[53] as well. In this report, it appears that higher Co oxide species (active species such as CoOOH) could be readily formed in the Ce-introduced catalyst, enhancing OER catalytic activity. When we deposited too small of an amount of Ce, the activity was reduced and vice versa (see Figure S12), emphasizing an optimal coverage (or interface) of Ce for maximum performance. It is also remarkable that the effects of Ce were also obtained from VB analysis, as can be seen from Figure 8. It has been reported that the electrochemical activity can be changed in various Co oxidation states for different Co species due to the difference in their surface kinetics and electrochemical activity toward the OER.[46] For this reason, the VB data were collected at a potential of 1.4 V in the early stages (low overpotential range) of the OER (before Co entirely

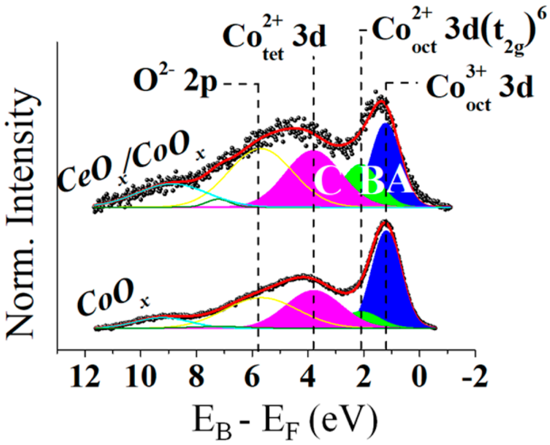

Figure 8. Valence bands for CoO$_x$ and CeO$_x$/CoO$_x$ at 1.4 V. The Co fitting results are labeled as A (blue), B (green), and C (pink), respectively, for the calculation of relative area ratios. The data were collected using a photon energy of 130 eV for the valence band. A Shirley background was subtracted from the spectrum before deconvolution.

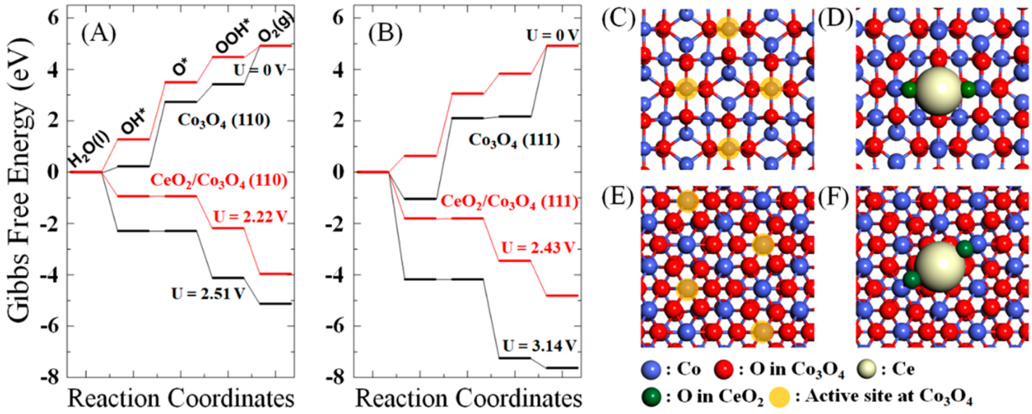

Figure 9. Gibbs free energy diagram for OER with the Co_3O_4 and CeO_2/Co_3O_4 systems with (A) (110) and (B) (111) surfaces. Slab models with the active site highlighted in orange: (C) Co_3O_4 (110), (D) CeO_2/Co_3O_4 (110), (E) Co_3O_4 (111), and (F) CeO_2/Co_3O_4 (111).

transforms to a higher Co valence state) and rigorously deconvoluted using fitting parameters reported in ref 52.

The raw data were assigned to Co^{2+}_{tet} (tetrahedral site, at 3.8 eV) and Co^{3+}_{oct} (octahedral site, at 1.2 eV) species from the spinel structure of Co_3O_4 and octahedral Co^{2+}_{oct} (at 2.1 eV) from $Co(OH)_2$[52] in the vicinity of the Fermi level (at 0 eV). Liu et al. recently found that Co^{2+}_{tet} and Co^{3+}_{oct} in spinel Co_3O_4 differ from each other in their surface kinetics and electrochemical activity for the OER. In particular, Co^{2+}_{tet} on the spinel Co_3O_4 surface is responsible for the formation of CoOOH,[54] which plays a significantly important role for a highly active OER catalyst.[55] The relative atomic ratio of $Co^{2+}_{tet}/Co^{3+}_{oct}$ on the Co_3O_4 surface of the samples can be calculated by comparing the area ("C/A" in Figure 8). The $Co^{2+}_{tet}/Co^{3+}_{oct}$ ratio in CeO_x/CoO_x (1.27) was larger than that for the CoO_x film (0.73) at the same OER potential, indicating that Co_3O_4 in CeO_x/CoO_x can readily transform to the active species, CoOOH. Furthermore, the relative amount of Co^{2+}_{oct} species in the $Co(OH)_2$ phase (area of "B″" in Figure 8) was significantly larger in the CeO_x/CoO_x film than in the CoO_x film, which also could improve the OER activity since $Co(OH)_2$ can transform into CoOOH, acting as a starting Co oxide phase.[52] These findings show a clear trend involving Co electronic structure variation through the introduction of Ce, enhancing the OER activity via the bifunctionality.

To further understand the specific role of Ce at Ce−Co interfaces, we calculated reaction energy diagrams for the CoO_x and CeO_x/CoO_x systems, as shown in Figure 9. We put an isolated CeO_2 cluster on the Co_3O_4 (110) and (111) surfaces, appropriate for the extremely small amounts of CeO_2 (1%) that are well dispersed on the Co_3O_4 in the experiments. Our calculations show that the binding energies of single CeO_2 clusters on the Co_3O_4 (110) and (111) surfaces are −4.07 and −5.20 eV, respectively, which are sufficiently negative to stabilize the system. All intermediates for OER including O* and OH* were calculated using the four systems Co_3O_4 (110), Co_3O_4 (111), CeO_2/Co_3O_4 (110), and CeO_2/Co_3O_4 (111), although we used the standard linear relationship between OH* and OOH*[56] binding to describe the energy of the OOH* intermediates. The reaction energy diagrams, based on the binding energies of the intermediates, are shown in Figure 9A,B; each system has the same rate-limiting step for OH* to O*, having the highest energy difference.

Interestingly, we show that the CeO_2/Co_3O_4 system requires a lower operating potential than Co_3O_4, regardless of which surface is considered, due to weaker intermediate binding energies and a reduced energy difference between OH* and O* in comparison to those of the Co_3O_4 system. The stable position of the CeO_2 cluster coincides with the strongest binding site for O* and OH* (highlighted in orange in Figure 9C,E), indicating that the CeO_2 cluster can block the original active sites and make new active sites having weaker binding energy that are favorable for the OER in comparison to the original Co_3O_4 system.

CONCLUSIONS

In summary, we have demonstrated a simple but novel bifunctional electrocatalyst based on a highly dense CeO_x/CoO_x catalyst fabricated via a two-step electrodeposition of Co (starting with Co seed formation). The electrocatalytic performance of CoO_x was enhanced by its highly dense nanosheet morphology and further improved through the bifunctionality introduced by Ce. The CoO_x catalyst showed good and stable activity (η = 0.331 V) for the OER; however, superior activity was observed for the CeO_x/CoO_x electrocatalyst (η = 0.313 V at 10 mA cm^{-2}). In order to understand this synergistic effect between Co and Ce, the CoO_x and CeO_x/CoO_x samples were further studied by synchrotron-based X-ray photoemission spectroscopy, which revealed that Ce promotes effective formation to CoOOH on the CoO_x catalyst by perturbing the electronic structure of surface Co species (Co_3O_4 and $Co(OH)_2$)). This Co electronic structure variation leads to a CeO_x/CoO_x catalyst that is more active than the CoO_x alone. Additionally, the DFT calculations provide insights into the mechanism for enhanced OER in the CeO_x/CoO_x. This consideration of catalytic synergy will possibly provide directions in the design of highly active OER electrocatalysts.

ASSOCIATED CONTENT

Supporting Information

The Supporting Information is available free of charge on the ACS Publications website at DOI: 10.1021/acscatal.8b00820.

Figures S1−S13 and Table S1 as described in the text (PDF)

AUTHOR INFORMATION

Corresponding Author

*E-mail for C.B.M.: mullins@che.utexas.edu.

ORCID

Kenta Kawashima: 0000-0001-7318-6115
Duck Hyun Youn: 0000-0001-7338-6715
Jie Lin: 0000-0002-1281-9713
Yang Liu: 0000-0002-7240-1546
Graeme Henkelman: 0000-0002-0336-7153
C. Buddie Mullins: 0000-0003-1030-4801

Notes

The authors declare no competing financial interest.

ACKNOWLEDGMENTS

This work was supported by the Welch Foundation through grants F-1436 and F-1841, and by the National Science Foundation via grant CHE-1664941. We also acknowledge the Pohang Accelerator Laboratory for acquisition of the HR-PES and the Texas Advanced Computing Center for computational resources.

REFERENCES

(1) Suen, N.-T.; Hung, S.-F.; Quan, Q.; Zhang, N.; Xu, Y.-J.; Chen, H. M. Electrocatalysis for the Oxygen Evolution Reaction: Recent Development and Future Perspectives. *Chem. Soc. Rev.* **2017**, *46*, 337−365.

(2) Zhang, H.; Zhang, Z.; Li, N.; Yan, W.; Zhu, Z. Cu$_2$O@C Core/shell Nanoparticle as an Electrocatalyst for Oxygen Evolution Reaction. *J. Catal.* **2017**, *352*, 239−245.

(3) Huan, T. N.; Rousse, G.; Zanna, S.; Lucas, I. T.; Xu, X.; Menguy, N.; Mougel, V.; Fontecave, M. A Dendritic Nanostructured Copper Oxide Electrocatalyst for the Oxygen Evolution Reaction. *Angew. Chem., Int. Ed.* **2017**, *56*, 4792−4796.

(4) Fan, K.; Ji, Y.; Zou, H.; Zhang, J.; Zhu, B.; Chen, H.; Daniel, Q.; Luo, Y.; Yu, J.; Sun, L. Hollow Iron−Vanadium Composite Spheres: A Highly Efficient Iron-Based Water Oxidation Electrocatalyst without the Need for Nickel or Cobalt. *Angew. Chem., Int. Ed.* **2017**, *56*, 3289−3293.

(5) Burke, M. S.; Enman, L. J.; Batchellor, A. S.; Zou, S.; Boettcher, S. W. Oxygen Evolution Reaction Electrocatalysis on Transition Metal Oxides and (Oxy)hydroxides: Activity Trends and Design Principles. *Chem. Mater.* **2015**, *27*, 7549−7558.

(6) Maiyalagan, T.; Jarvis, K. A.; Therese, S.; Ferreira, P. J.; Manthiram, A. Spinel-type Lithium Cobalt Oxide as a Bifunctional Electrocatalyst for the Oxygen Evolution and Oxygen Reduction Reactions. *Nat. Commun.* **2014**, *5*, 3949.

(7) Grimaud, A.; Diaz-Morales, O.; Han, B.; Hong, W. T.; Lee, Y.-L.; Giordano, L.; Stoerzinger, K. A.; Koper, M. T. M.; Shao-Horn, Y. Activating Lattice Oxygen Redox Reactions in Metal Oxides to Catalyse Oxygen Evolution. *Nat. Chem.* **2017**, *9*, 457−465.

(8) Suntivich, J.; May, K. J.; Gasteiger, H. A.; Goodenough, J. B.; Shao-Horn, Y. A Perovskite Oxide Optimized for Oxygen Evolution Catalysis from Molecular Orbital Principles. *Science* **2011**, *334*, 1383−1385.

(9) Mabayoje, O.; Shoola, A.; Wygant, B. R.; Mullins, C. B. The Role of Anions in Metal Chalcogenide Oxygen Evolution Catalysis: Electrodeposited Thin Films of Nickel Sulfide as “Pre-catalysts. *ACS Energy Lett.* **2016**, *1*, 195−201.

(10) Tang, C.; Cheng, N.; Pu, Z.; Xing, W.; Sun, X. NiSe Nanowire Film Supported on Nickel Foam: An Efficient and Stable 3D Bifunctional Electrode for Full Water Splitting. *Angew. Chem., Int. Ed.* **2015**, *54*, 9351−9355.

(11) Xiao, X.; He, C.-T.; Zhao, S.; Li, J.; Lin, W.; Yuan, Z.; Zhang, Q.; Wang, S.; Dai, L.; Yu, D. A General Approach to Cobalt-based Homobimetallic Phosphide Ultrathin Nanosheets for Highly Efficient Oxygen Evolution in Alkaline Media. *Energy Environ. Sci.* **2017**, *10*, 893−899.

(12) Duan, H.; Li, D.; Tang, Y.; He, Y.; Ji, S.; Wang, R.; Lv, H.; Lopes, P. P.; Paulikas, A. P.; Li, H.; Mao, S. X.; Wang, C.; Markovic, N. M.; Li, J.; Stamenkovic, V. R.; Li, Y. High-Performance Rh$_2$P Electrocatalyst for Efficient Water Splitting. *J. Am. Chem. Soc.* **2017**, *139*, 5494−5502.

(13) Anantharaj, S.; Reddy, P. N.; Kundu, S. Core-Oxidized Amorphous Cobalt Phosphide Nanostructures: An Advanced and Highly Efficient Oxygen Evolution Catalyst. *Inorg. Chem.* **2017**, *56*, 1742−1756.

(14) Jiang, N.; You, B.; Sheng, M.; Sun, Y. Electrodeposited Cobalt-Phosphorous-Derived Films as Competent Bifunctional Catalysts for Overall Water Splitting. *Angew. Chem., Int. Ed.* **2015**, *54*, 6251−6254.

(15) Wang, Z.; Li, J.; Tian, X.; Wang, X.; Yu, Y.; Owusu, K. A.; He, L.; Mai, L. Porous Nickel−Iron Selenide Nanosheets as Highly Efficient Electrocatalysts for Oxygen Evolution Reaction. *ACS Appl. Mater. Interfaces* **2016**, *8*, 19386−19392.

(16) Xu, X.; Song, F.; Hu, X. A Nickel Iron Diselenide-derived Efficient Oxygen-Evolution Catalyst. *Nat. Commun.* **2016**, *7*, 12324−12330.

(17) Chen, W.; Liu, Y. Y.; Li, Y. Z.; Sun, J.; Qiu, Y. C.; Liu, C.; Zhou, G. M.; Cui, Y. In Situ Electrochemically Derived Nanoporous Oxides from Transition Metal Dichalcogenides for Active Oxygen Evolution Catalysts. *Nano Lett.* **2016**, *16*, 7588−7596.

(18) Yin, H. J.; Tang, Z. Y. Ultrathin Two-dimensional Layered Metal Hydroxides: an Emerging Platform for Advanced Catalysis, Energy Conversion and Storage. *Chem. Soc. Rev.* **2016**, *45*, 4873−4891.

(19) Song, F.; Hu, X. Exfoliation of Layered Double Hydroxides for Enhanced Oxygen Evolution Catalysis. *Nat. Commun.* **2014**, *5*, 4477.

(20) Zeng, Z.; Chang, K.-C.; Kubal, J.; Markovic, N. M.; Greeley, J. Stabilization of Ultrathin (hydroxy)oxide Films on Transition Metal Substrates for Electrochemical Energy Conversion. *Nat. Energy* **2017**, *2*, 17070−17078.

(21) Chen, G.; Zhao, Y.; Fu, G.; Duchesne, P. N.; Gu, L.; Zheng, Y.; Weng, X.; Chen, M.; Zhang, P.; Pao, C.-W.; Lee, J.-F.; Zheng, N. Interfacial Effects in Iron-Nickel Hydroxide-Platinum Nanoparticles Enhance Catalytic Oxidation. *Science* **2014**, *344*, 495−499.

(22) Ng, J. W. D.; García-Melchor, M.; Bajdich, M.; Chakthranont, P.; Kirk, C.; Vojvodic, A.; Jaramillo, T. F. Gold-supported Cerium-doped NiO$_x$ Catalysts for Water Oxidation. *Nat. Energy* **2016**, *1*, 16053−16060.

(23) Liu, Z.; Li, N.; Zhao, H.; Zhang, Y.; Huang, Y.; Yin, Z.; Du, Y. Regulating the Active Species of Ni(OH)$_2$ using CeO$_2$: 3D CeO$_2$/Ni(OH)$_2$/carbon Foam as an Efficient Electrode for the Oxygen Evolution Reaction. *Chem. Sci.* **2017**, *8*, 3211−3217.

(24) Lim, H.; Kim, J. Y.; Evans, E. J.; Rai, A.; Kim, J.-H.; Wygant, B. R.; Mullins, C. B. Activation of a Nickel-based OER Catalyst on a Hematite Photoanode via Incorporation of Cerium for Photoelectrochemical Water Oxidation. *ACS Appl. Mater. Interfaces* **2017**, *9*, 30654−30661.

(25) Feng, J.-X.; Ye, S.-H.; Xu, H.; Tong, Y.-X.; Li, G.-R. Design and Synthesis of FeOOH/CeO$_2$ Heterolayered Nanotube Electrocatalysts for the Oxygen Evolution Reaction. *Adv. Mater.* **2016**, *28*, 4698−4703.

(26) Esch, F.; Fabris, S.; Zhou, L.; Montini, T.; Africh, C.; Fornasiero, P.; Comelli, G.; Rosei, R. Electron Localization Determines Defect Formation on Ceria Substrates. *Science* **2005**, *309*, 752−755.

(27) Zheng, Y.-R.; Gao, M.-R.; Gao, Q.; Li, H.-H.; Xu, J.; Wu, Z.-Y.; Yu, S.-H. An Efficient CeO$_2$/CoSe$_2$ Nanobelt Composite for Electrochemical Water Oxidation. *Small* **2015**, *11*, 182−188.

(28) Kresse, G.; Furthmuller, J. Efficient Iterative Schemes for ab initio Total-energy Calculations using a Plane-wave Basis Set. *Phys. Rev. B: Condens. Matter Mater. Phys.* **1996**, *54*, 11169−11186.

(29) Dudarev, S. L.; Botton, G. A.; Savrasov, S. Y.; Humphreys, C. J.; Sutton, A. P. Electron-energy-loss Spectra and the Structural Stability of Nickel Oxide: An LSDA+U Study. *Phys. Rev. B: Condens. Matter Mater. Phys.* **1998**, *57*, 1505−1509.

(30) Kim, H. Y.; Lee, H. M.; Henkelman, G. CO Oxidation Mechanism on CeO$_2$-Supported Au Nanoparticles. *J. Am. Chem. Soc.* **2012**, *134*, 1560−1570.

(31) Wang, L.; Maxisch, T.; Ceder, G. Oxidation Energies of Transition Metal Oxides within the GGA+U Framework. *Phys. Rev. B: Condens. Matter Mater. Phys.* **2006**, *73*, 195107.

(32) Perdew, J. P.; Burke, K.; Ernzerhof, M. Generalized Gradient Approximation Made Simple. *Phys. Rev. Lett.* **1996**, *77*, 3865−3868.

(33) Yoon, K. R.; Shin, K.; Park, J.; Cho, S.-H.; Kim, C.; Jung, J.-W.; Cheong, J. Y.; Byon, H. R.; Lee, H. M.; Kim, I.-D. Brush-Like Cobalt Nitride Anchored Carbon Nanofiber Membrane: Current Collector-Catalyst Integrated Cathode for Long Cycle Li−O_2 Batteries. *ACS Nano* **2018**, *12*, 128−139.

(34) Murthy, N. S.; Bednarczyk, C.; Minor, H. Depth-profiles of Structure in Single- and Multilayered Commercial Polymer Films using Grazing-incidence X-ray Diffraction. *Polymer* **2000**, *41*, 277−284.

(35) Yang, W.; Gao, Z.; Ma, J.; Wang, J.; Zhang, X.; Liu, L. Two-step Electrodeposition Construction of Flower-on-sheet Hierarchical Cobalt Hydroxide Nano-forest for High-capacitance Supercapacitors. *Dalton Trans.* **2013**, *42*, 15706−15715.

(36) Casella, I. G.; Guascito, M. R. Anodic Electrodeposition of Conducting Cobalt Oxyhydroxide Films on a Gold Surface: XPS Study and Electrochemical Behaviour in Neutral and Alkaline Solution. *J. Electroanal. Chem.* **1999**, *476*, 54−63.

(37) Casella, I. G.; Gatta, M. Study of the Electrochemical Deposition and Properties of Cobalt Oxide Species in Citrate Alkaline Solutions. *J. Electroanal. Chem.* **2002**, *534*, 31−38.

(38) Palmas, S.; Ferrara, F.; Vacca, A.; Mascia, M.; Polcaro, A. M. Behavior of Cobalt Oxide Electrodes during Oxidative Processes in Alkaline Medium. *Electrochim. Acta* **2007**, *53*, 400−406.

(39) Liu, R.; Hull, S.; Fayek, M. A New Approach to Measuring D/H Ratios with the Cameca IMS-7F. *Surf. Interface Anal.* **2011**, *43*, 458−461.

(40) Burke, L. D.; Lyons, M. E.; Murphy, O. J. Formation of Hydrous Oxide Films on Cobalt under Potential Cycling Conditions. *J. Electroanal. Chem. Interfacial Electrochem.* **1982**, *132*, 247−261.

(41) Sun, Y.; Gao, S.; Lei, F.; Liu, J.; Liang, L.; Xie, Y. Atomically-thin Non-layered Cobalt Oxide Porous Sheets for Highly Efficient Oxygen-evolving Electrocatalysts. *Chem. Sci.* **2014**, *5*, 3976−3982.

(42) Naumkin, A. V.; Ivanova, T. M.; Shchukarev, A. V.; Sidorov, A. A.; Kiskin, M. A.; Eremenko, I. L. X-ray Photoelectron Spectra of Cobalt Trimethylacetates. *Dokl. Chem.* **2006**, *411*, 234−239.

(43) Seah, M. P. An Accurate and Simple Universal Curve for the Energy-dependent Electron Inelastic Mean Free Path. *Surf. Interface Anal.* **2012**, *44*, 497−503.

(44) Carenco, S.; Wu, C. H.; Shavorskiy, A.; Alayoglu, S.; Somorjai, G. A.; Bluhm, H.; Salmeron, M. Synthesis and Structural Evolution of Nickel-Cobalt Nanoparticles Under H_2 and CO_2. *Small* **2015**, *11*, 3045−3053.

(45) Clemens, W.; Vescovo, E.; Kachel, T.; Carbone, C.; Eberhardt, W. Spin-resolved Photoemission Study of the Reaction of O_2 with fcc Co(100). *Phys. Rev. B: Condens. Matter Mater. Phys.* **1992**, *46*, 4198−4204.

(46) McIntyre, N. S.; Cook, M. G. X-ray Photoelectron Studies on Some Oxides and Hydroxides of Cobalt, Nickel, and Copper. *Anal. Chem.* **1975**, *47*, 2208−2213.

(47) Gao, Y.; Chen, D.; Chen, C.; Shao, Z.; Ciucci, F. Oriented $PrBaCo_2O_{5+\delta}$ Thin Films for Solid Oxide Fuel Cells. *J. Power Sources* **2015**, *278*, 623−629.

(48) Bruix, A.; Rodriguez, J. A.; Ramírez, P. J.; Senanayake, S. D.; Evans, J.; Park, J. B.; Stacchiola, D.; Liu, P.; Hrbek, J.; Illas, F. A New Type of Strong Metal−Support Interaction and the Production of H_2 through the Transformation of Water on Pt/CeO_2(111) and Pt/CeOx/TiO_2(110) Catalysts. *J. Am. Chem. Soc.* **2012**, *134*, 8968−8974.

(49) Suchorski, Y.; Wrobel, R.; Becker, S.; Weiss, H. CO Oxidation on a CeO_x/Pt(111) Inverse Model Catalyst Surface: Catalytic Promotion and Tuning of Kinetic Phase Diagrams. *J. Phys. Chem. C* **2008**, *112*, 20012−20017.

(50) Yang, F.; Graciani, J.; Evans, J.; Liu, P.; Hrbek, J.; Sanz, J. F.; Rodriguez, J. A. CO Oxidation on Inverse CeO_x/Cu(111) Catalysts: High Catalytic Activity and Ceria-Promoted Dissociation of O_2. *J. Am. Chem. Soc.* **2011**, *133*, 3444−3451.

(51) Burch, R. Gold Catalysts for Pure Hydrogen Production in the Water-gas Shift Reaction: Activity, Structure and Reaction Mechanism. *Phys. Chem. Chem. Phys.* **2006**, *8*, 5483−5500.

(52) Favaro, M.; Yang, J.; Nappini, S.; Magnano, E.; Toma, F. M.; Crumlin, E. J.; Yano, J.; Sharp, I. D. Understanding the Oxygen Evolution Reaction Mechanism on CoO_x using Operando Ambient-Pressure X-ray Photoelectron Spectroscopy. *J. Am. Chem. Soc.* **2017**, *139*, 8960−8970.

(53) Li, N.; Bediako, D. K.; Hadt, R. G.; Hayes, D.; Kempa, T. J.; von Cube, F.; Bell, D. C.; Chen, L. X.; Nocera, D. G. Influence of Iron Doping on Tetravalent Nickel Content in Catalytic Oxygen Evolving Films. *Proc. Natl. Acad. Sci. U. S. A.* **2017**, *114*, 1486−1491.

(54) Wang, H.-Y.; Hung, S.-F.; Chen, H.-Y.; Chan, T.-S.; Chen, H. M.; Liu, B. In Operando Identification of Geometrical-Site-Dependent Water Oxidation Activity of Spinel Co_3O_4. *J. Am. Chem. Soc.* **2016**, *138*, 36−39.

(55) Tung, C.-W.; Hsu, Y.-Y.; Shen, Y.-P.; Zheng, Y.; Chan, T.-S.; Sheu, H.-S.; Cheng, Y.-C.; Chen, H. M. Reversible Adapting Layer Produces Robust Single-crystal Electrocatalyst for Oxygen Evolution. *Nat. Commun.* **2015**, *6*, 8106.

(56) Man, I. C.; Su, H.-Y.; Calle-Vallejo, F.; Hansen, H. A.; Martinez, J. I.; Inoglu, N. G.; Kitchin, J.; Jaramillo, T. F.; Norskov, J. K.; Rossmeisl, J. Universality in Oxygen Evolution Electrocatalysis on Oxide Surfaces. *ChemCatChem* **2011**, *3*, 1159−1165.